Received: 12 May 2023 | Revised: 9 August 2023 | Accepted: 10 August 2023

DOI: 10.1111/jace.19429

Journal of the American Ceramic Society

RESEARCH ARTICLE

A comparative study of cerium oxides formed by pulsed laser ablation and continuous wave laser heating

Alexander W. Auner[1,2] | **Mark A. Burton**[3] | **Lauren A. Nagel**[1,4] | **Jonathan C. Crowhurst**[1] | **David G. Weisz**[1] | **Kimberly B. Knight**[1]

[1]Nuclear and Chemical Science Division, Lawrence Livermore National Laboratory, Livermore, California, USA

[2]Department of Physics, Boston College, Chestnut Hill, Massachusetts, USA

[3]Materials Science Division, Lawrence Livermore National Laboratory, Livermore, California, USA

[4]Nuclear Engineering and Radiological Sciences, University of Michigan, Ann Arbor, Michigan, USA

Correspondence
Alexander W. Auner, Department of Physics, Boston College, Chestnut Hill, MA 02467, USA.
Email: auner@bc.edu

Funding information
Lawrence Livermore National Laboratoryc, Grant/Award Number: DE-AC52-07NA27344; Laboratory Directed Research and Development, Grant/Award Number: 20-SI-006

Abstract

The formation of Ce_2O_3 from cerium metal requires complex reducing conditions. Alternatively, we show that different stoichiometries and structures of cerium oxides can be generated in high-temperature laser experiments by varying the availability of oxygen and the use of either pulsed laser ablation (PLA) or continuous wave (CW) laser heating of cerium metal. X-ray diffraction and Raman spectroscopy suggest that a low structural order Ce_2O_3/CeO_2 mixed structure is formed in a 1% O_2 atmosphere with PLA. For CW heating in a 1% O_2 environment, Raman measurements show the formation of crystalline A-type Ce_2O_3 in proximity to the point of laser impingement. These experiments were repeated in $^{18}O_2$ and allowed us to report for the first time the corresponding Raman spectrum of $Ce_2{}^{18}O_3$.

KEYWORDS

cerium/cerium compounds, deposition, Raman spectroscopy, X-ray methods

1 | INTRODUCTION

Lanthanides in the form of R_2O_3 (sesquioxides) have been extensively studied, but the study of Ce_2O_3 is limited. Ce_2O_3 exhibits some unique properties, such as giant magnetocapacitance[1] and excellent reducing properties resulting from a low affinity for oxygen vacancies due to the complete reduction of Ce atoms to Ce^{3+}, forming a hexagonal (A-type) structure.[2] This configuration has been investigated theoretically as a good potential agent for hydrogenation catalysis.[2] Some additional recent examples focusing on ceria and related systems are adjusting oxygen vacancies by engineering amorphous cerium oxides, which have the property of increasing active sites and dangling bonds useful in nitrogen fixation,[3] synthesis via pulsed laser ablation (PLA) that mixes fluorite/sesquioxide structure,[4] or adding lanthanum to synthesized cerium oxides.[5]

CeO_{2-x} was synthesized using several different methods, including processing in plasma reactors,[6] via chemical reactions,[6] heating in the presence of H_2 or low O_2 partial pressure,[7] thin-film annealing,[8] electrolysis,[9] and laser-induced plasmas.[4] Methods for bulk Ce_2O_3 synthesis range from more complex multi-step annealing processes

involving reduction using a hydrogen intermediate,[10,11] reduction of CeO_2 by Ce at 1500°C heating in an induction furnace,[12] or by removing oxygen in an ultrahigh vacuum at 727°C.[13] The difference in local temperature (~1000 K for continuous wave [CW] heating[14]) and heating and cooling times between PLA and CW heating results in potentially different stoichiometries. CW heating has synthesized unique oxide stoichiometries of, for example, vanadium,[15,16] tantalum,[17,18] and has additionally been applied to the synthesis of various other metal oxides.[14] For CW vanadium oxidation, it was found that oxide formation occurred in the liquid phase, which cooled into either polycrystalline or single crystal states depending on irradiation time.[16] Oxidation by laser offers the advantages of localized heating with extreme heating and cooling rates. The previous work varying atmospheric conditions and formation of metal oxides by nonequilibrium conditions motivated us to show that hexagonal Ce_2O_3 can be formed under a novel set of conditions—a bottom–up synthesis method of formation from pure cerium using limited oxygen availability coupled with CW laser heating.

As pointed out by Filotti et al.,[19] Ceria's reversible redox cycle allows oxygen atoms to be mobile within the lattice. When oxygen atoms vacate the ceria lattice, they give rise to a large variety of non-stoichiometric oxides between CeO_2 and Ce_2O_3.[19] The transition between Ce^{3+} and Ce^{4+} ions and vacancy formation has been demonstrated at low oxygen pressures with varying annealing times and temperatures.[13,19] Variations in bond length or the formation of oxygen vacancy defects lead to changes in molecular vibrational frequency that are detectable in Raman spectra, as indicated by Schmitt et al.[20] Raman spectroscopy is a powerful characterization tool that has been used to probe complex cerium oxide local structures[21] and the chemical properties of defects from dopant ions and oxygen vacancies.[20,22–24] In this work, we produce different structures of cerium oxide using PLA and CW laser heating of a solid target in low-oxygen atmospheres. We use Raman spectroscopy to characterize hexagonal cerium sesquioxide formed by laser heating and an amorphous or poorly crystallized cerium oxide formed from PLA along with X-ray diffraction, which is in good agreement with previous work.[4]

2 | MATERIALS AND METHODS

A dual-laser platform was used in this study. PLA experiments used a Q-switched Nd:YAG pulsed laser (Quantel Ultra 100, 1064 nm, shot frequency of 20 Hz, pulse width of 7 ns) focused on a single spot for 10 min (~12 000 pulses). The laser was focused to a spot size of approximately 300 μm with a 10 cm biconvex lens, with an energy measured to be 50 mJ at the sample position (intensity of approximately 2×10^9 W/cm^2). For CW heating, a 1064 nm laser (IPG Photonics) was focused by the same focusing lens to a spot size of approximately 200 μm and estimated to be 30 W at the sample surface, resulting in an approximate intensity of 1×10^5 W/cm^2. Either a polished NaCl or silicon substrate was placed approximately 3 cm in front of the cerium surface to collect the particulates in similar fashion to Pereira et al.[4] The dwell time for CW heating was 1 min on a single spot. The lasers were focused through a polished sapphire window into a sealed vacuum chamber where the cerium target was clipped to a linear translator (see Burton et al.[25] for a schematic of the chamber set-up).

Cerium foil (1 mm thick, 99.9% purity, Sigma–Aldrich) was mechanically polished with diamond polish followed by 0.1 μm silica bead colloidal solution. The sample was then immediately evacuated in a vacuum chamber to <30 mTorr. Consecutive experiments on different cerium samples were each conducted by backfilling the chamber to 760 Torr with oxygen mixtures of different concentrations—deficient oxygen (pre-mixed 1% $^{16}O_2$, 99.99% Ar, Matheson) and pure O_2 (99%, Sigma–Aldrich) for PLA and abundant oxygen (20% O_2, 80% Ar) and deficient oxygen (1% O_2, 99% Ar) for CW heating. Isotopic shift experiments were also conducted on separate polished cerium samples in a 1% $^{18}O_2$ (99%, Sigma–Aldrich) and Ar (99.999%, Sigma–Aldrich) mixture, which was produced by mixing pure argon and oxygen isotope canisters and reading the line pressure sensor to ±0.5% uncertainty.

After the PLA or CW heating, the chamber was evacuated to prevent potential oxidation and transferred to an XYZ linear micrometer translation stage within the Raman system. The chamber was oriented such that the sapphire window was facing a 20× microscope objective (Mitutoyo apochromatic), which was used to survey the cerium surface and collect scattered light. The ablated cerium surface was translated forward to within 2 mm of the internal surface of the sapphire window. Particulates were imaged by white light illumination of the cerium surface and then targeted with the 632.8 nm HeNe (Melles Griot LHR Laser Tube) Raman excitation laser. Particles analyzed had a diameter approximately equal to or greater than the focused laser ~10 μm spot diameter. The excitation laser power was less than approximately 10 mW at the sample surface. Backscattered light was collected through the objective and passed through three laser rejection filters. Spectra were recorded with a Princeton Instruments Acton SP2300 spectrometer coupled with a Pixis 400 detector, first at 300 lines/mm grating and additionally at 1800 lines/mm. The spectrometer was calibrated using multiple lines from a neon lamp. The estimated accuracy of this procedure was ±1 and ±2 cm^{-1} for the 1800 and 300 lines/mm grating, respectively. Acquisition times and accumulations were set to a maximum of 60 s and 10 accumulations, respectively, and were

chosen depending on signal strength. Because spectral comparisons were made over a small wavenumber window, correction for instrument response was unnecessary. Spectra were processed by removal of background light and cosmic rays, where necessary. For comparison purposes, some spectra were normalized in such a manner that the highest peak was set to 1 and lowest point to 0. A CeO_2 ceramic sputtering target (Kurt Lesker) was used as a reference standard.

Particulates formed in 1% O_2 and 99.99% Ar from PLA were collected on a single crystal silicon plate for low background X-ray diffraction (XRD) measurements. The plate was then mounted onto a polymethyl methacrylate sample holder and analyzed on a Bruker AXS D8 ADVANCE X-ray diffractometer equipped with a LynxEye one-dimensional linear Si strip detector with Bruker DIFFRAC.EVA V5 software package used for data analysis. The scan parameters were 20°–80° 2θ with a 0.02° step and 3 s counting time per step with a 0.6° divergence slit and the Lynx Iris set to 13 mm position. The X-ray source was Ni-filtered Cu radiation from a sealed tube operated at 40 kV and 40 mA.

Following Raman measurements of the metal surface, the cerium foil was characterized by secondary electron mode of an FEI Inspect F50 scanning electron microscope to survey surface morphology corresponding to the different particulates near within the crater itself up to within 20 μm of the edge and further away. The accelerating voltages were 15 and 20 kV for surface imaging following PLA and CW heating, respectively, and 11.5 mm working distance was maintained for all images.

3 | RESULTS

Changes to laser type (PLA vs. CW) led to observable differences in particulate appearance both near and away from the crater formed at the point of laser impingement. Figure 1a shows a secondary electron image of the damage area (crater) produced by CW heating in an oxygen-deficient atmosphere. The CW laser produced two morphologically distinct populations of particulates indicated by red and blue arrows in Figure 1b. The first population, indicated by the red arrow on the left side of the image, was found in the crater and identified by the qualitative change in topology indicated by the lighter gray tint. These spherical particulates are scattered throughout the smooth melt. The second population, indicated by the blue arrow, consists of non-spherical particles scattered around the outside of the crater. PLA of cerium foil in an oxygen-deficient atmosphere also formed a hemispherical crater (Figure S1) in addition to an abundance of ~1 μm spherical particles more than 500 μm away from the crater, as well as larger metallic spheres ~5 μm in diameter (Figure 1c). The features and size of the particulates found inside the PLA crater (Figure 1d) have a similar morphology to those found outside the crater for CW heating (Figure 1b, blue arrow), but vary greatly in cluster size.

3.1 | CW heating (away from the crater) and PLA (in the crater)

Particulates surveyed outside of the CW heated crater in Figure 1b (blue arrow) and in the PLA crater (Figure 1c) were identified as CeO_2 by the strong symmetric breathing Raman F_{2g} mode for the fluorite structure at approximately 461 cm^{-1} (Figure S2). The F_{2g} mode for these particulates as well as other cerium oxide particulates made here exhibited a shift to lower wavenumber than native oxide that naturally forms on the surface of cerium foil following long-term oxygen exposure of pure cerium measured before ablation or heating (Figure 2, blue) at 465 cm^{-1} in addition to broadening compared to the cerium sputtering target (Figure 2, black).[6,20,26]

The PLA experiment was conducted in a pure $^{18}O_2$ atmosphere to observe the spectral shift imparted by isotopic substitution. In the simplified case where we consider oscillating linear diatomic masses, the magnitude of the Raman isotopic shift can be determined from (see, e.g., Weckhuysen et al.[27]):

$$\nu_{18} \approx \nu_{16}\sqrt{\frac{\mu_{16}}{\mu_{18}}} \tag{1}$$

where ν is the Raman shifted signature in cm^{-1} and μ_{16} and μ_{18} are the relevant reduced masses given by

$$\mu = \frac{m_O m_{Ce}}{m_O + m_{Ce}} \tag{2}$$

where m_{Ce} is the mass of cerium and m_O is the mass of ^{16}O and ^{18}O. For the fluorite mode, the symmetric breathing vibration motion is of the oxygen atoms with the cerium atom remaining static, and hence the frequency is given by (see, e.g., Lv et al.[28])

$$\nu_{18} \approx \nu_{16}\sqrt{\frac{m_{16}}{m_{18}}} \tag{3}$$

This approximately 6% shift, corresponding to 26 cm^{-1}, is somewhat larger than our measured shift of ~18 cm^{-1}. Our value is consistent with a previously observed shift of ~17 cm^{-1} for 81 nm particles.[29]

3.2 | PLA (>1.5 crater diameters away from the crater center)

In an oxygen-deficient atmosphere, different particulates produced by PLA were found outside the crater edge

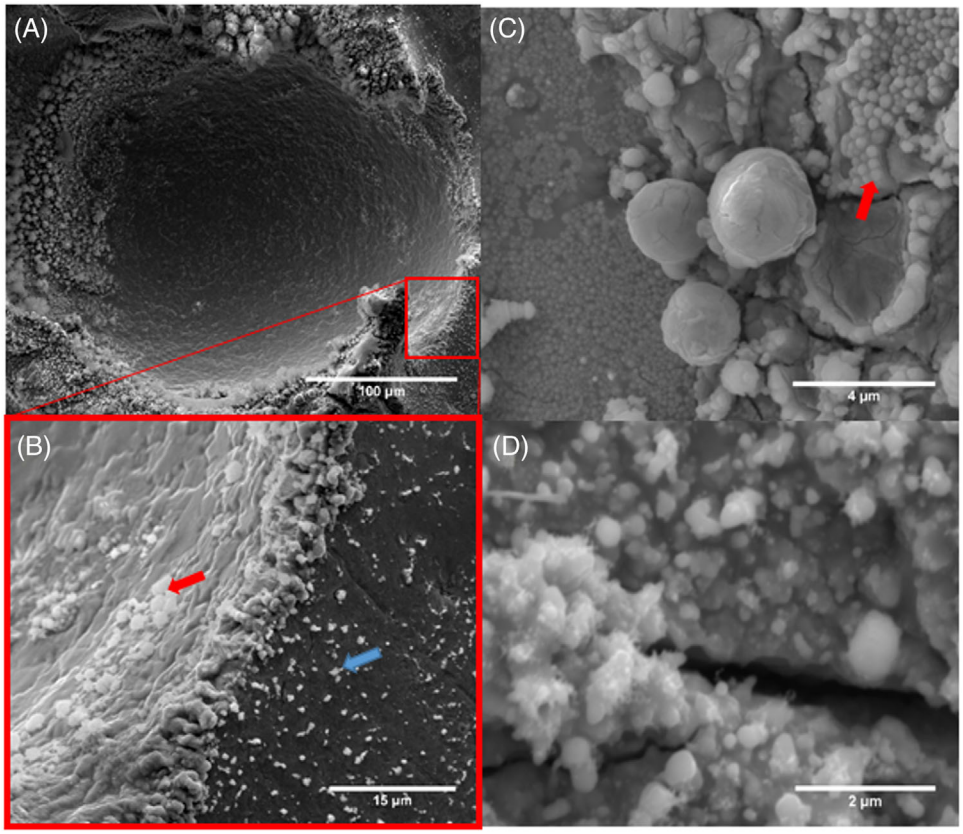

FIGURE 1 Secondary scanning electron microscopy (SEM) image of the cerium foil surface showing laser induced damage in an oxygen-deficient atmosphere and oxide formation. (a) Crater from continuous wave (CW) heating; (b) region of interest for the CW heating crater with red and blue arrows indicating two regions of distinct particulates; (c) pulsed laser ablation (PLA) outside the crater edge (particulates marked by a red arrow); (d) PLA inside the crater.

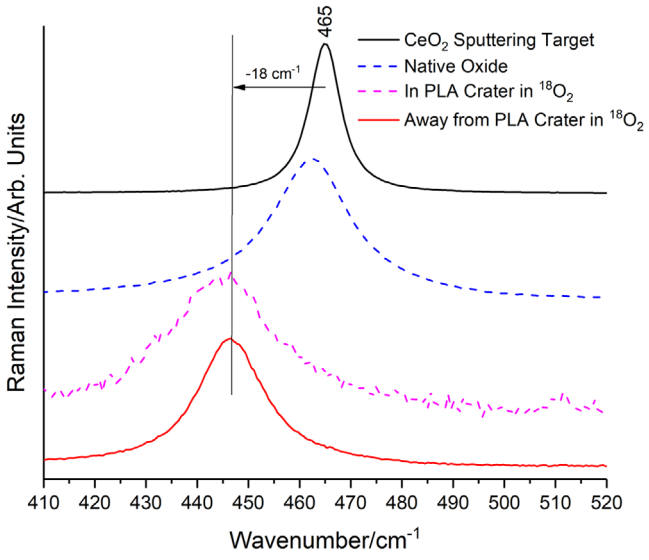

FIGURE 2 Raman isotopic shift comparison of particulates formed from pulsed laser ablation (PLA) in a pure $^{18}O_2$ atmosphere on a cerium metal surface ex situ to native oxide coating the unpolished cerium prior to ablation. Also shown for reference is a spectrum obtained spectrum from a CeO_2 sputtering target.

(Figure 1c, red arrow). These particulates had a Raman spectrum featuring additional broad lower wavenumber modes and a reduced fluorite mode relative to the F_{2g} mode from the native oxide when comparing the relative baseline intensity (Figure 3a, black). The broad modes of this particulate spectrum suggest low structural order. The same spectral signature was found from surveying nanocrystalline clusters of particulates collected from locations located toward the most particle dense center area on the NaCl substrate. The relative strength of the Raman modes was heterogeneous between different clusters on the film deposited on a NaCl substrate (Figure 3a, red and blue). When subjected to increasing CW Raman laser power, unlike particulate identified in the crater, these particulates were unstable when heated. A time dependent transformation was observed for laser powers tested (<10 mW) as a particulate was heated over seconds, and the ~461 cm^{-1} fluorite mode intensity increased in real time to match the intensity of the CeO_2 native oxide F_{2g} mode. This was also observed on apparently mostly cerium metal particulates formed following PLA in trace oxygen conditions in situ (>99.99% Ar). These particulates

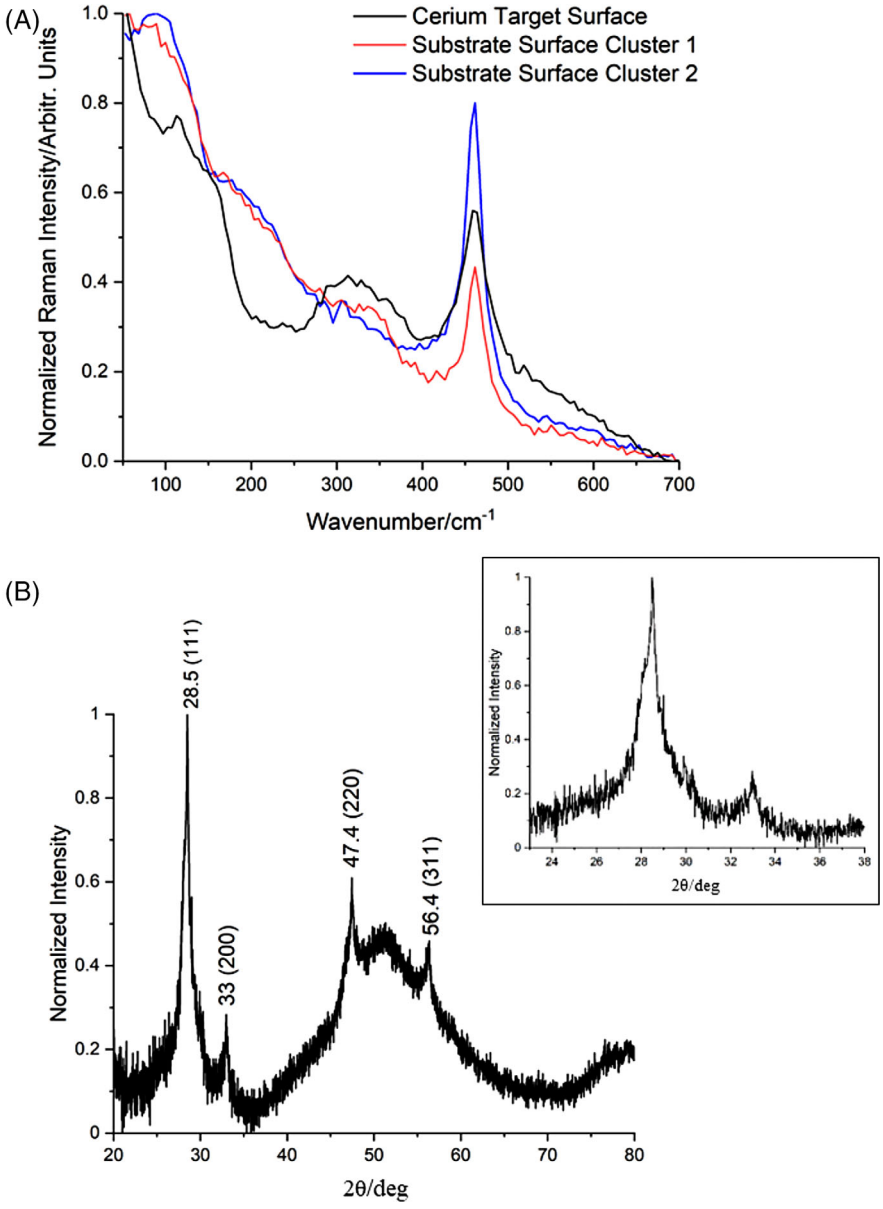

FIGURE 3 Characterization of particulate formed from pulsed laser ablation (PLA) in a 1% $^{16}O_2$ atmosphere. (a) Ex situ Raman measurements of particulates formed away from the point of laser impingement on the cerium metal surface and additionally of film collected on a NaCl substrate. (b) X-ray diffraction (XRD) pattern of the cerium oxide film collected on a silicon substrate with (inset) smaller scale of XRD pattern.

similarly exhibited an F_{2g} feature that formed and increased in intensity in real time.

The PLA experiment was repeated to collect particulates on Si for XRD characterization. Ex situ Raman spectra of these particulates match those collected on NaCl (with the additional Si Raman modes). The XRD pattern (Figure 3b) has clear peaks at $2\theta \sim 28.5°$, 33.0°, and 47.4° observed by Pereira et al.[4] following pulsed ablation of pure cerium and additionally 56.4° seen in the XRD pattern of an experiment of the annealing and crystallization of CeO_2 from an amorphous state[30] (Figure 3b). Furthermore, peaks at $2\theta \sim 28.5°$ and 33.1° that correspond to the (111) and (200) crystal orientations, respectively, exhibit a slightly broadened, irregular shape (Figure 3b, inset) consistent with multiple phases, including the defective poorly crystallized CeO_{2-x} or amorphous Ce_2O_3[4] or poorly crystallized or amorphous CeO_2[30] structure that was reported.

3.3 | CW heating (in the crater)

Additional cerium oxide particulates (Figure 1b, red arrow) were identified by their Raman spectrum in the crater produced by CW heating in a 1% oxygen atmosphere (Figure 4 and additional high-resolution spectra in Figure S3). The spectra include a somewhat downshifted fluorite

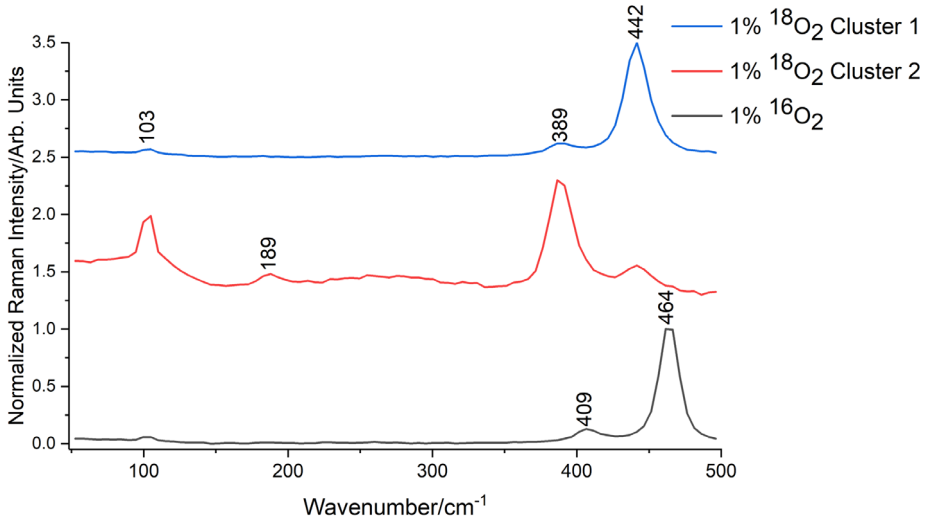

FIGURE 4 Raman spectra of particulate located around the point of continuous wave (CW) laser impingement in oxygen-deficient $^{16}O_2$ (black) and $^{18}O_2$ (red and blue) environments showing isotopic shifts.

mode, in addition to three new lower wavenumber modes (Figure 4). The 103 and 409 cm^{-1} modes are in good agreement with the anti-Stokes modes assigned to the hexagonal A-type crystalline Ce_2O_3 spectrum.[10,11] The 103 cm^{-1} was assigned to the E_g Ce–O(II) bend, and 409 cm^{-1} was assigned to a combination of A_{1g} stretch and more dominant shorter E_g Ce–O(II) bond stretch.[10,11] The presence of lower wavenumber modes is also present in surveyed particulate clusters formed in $^{18}O_2$ in the crater (Figure 4, blue and red). As seen, the relative intensity of the 442 and 389 cm^{-1} features, that is, CeO_2 to Ce_2O_3, suggests particle formation can be variable. The very weak Ce_2O_3 A_{1g} mode at 189 cm^{-1} can be discerned in the red trace of Figure 4. Of note, previous studies that heated pellets in the presence of H_2 gas did not see the F_{2g} fluorite mode.[10,11]

To confirm the accuracy of previously assigned Raman active modes, the CW heating experiment was conducted in a <1% $^{18}O_2$ and >99% Ar atmosphere to observe the spectral shift imparted by isotopic substitution. There is good agreement with the approximately 5% shift predicted from Equation (1) seen in higher wavenumber modes in our spectra. For example, from a corresponding high-resolution spectra, the E_g Ce–O(II) stretch shifts from 409 to 389 cm^{-1} (Figure 4). The direction of motion for the 103 cm^{-1} E_g bend (shown in Ref. [10]) is both Ce and O atoms moving in the same direction. This motion produces a Raman isotopic shift that would result from the approximate correction:

$$\upsilon_{18} \approx \upsilon_{16}\sqrt{\frac{m_{Ce}+m_{16}}{m_{Ce}+m_{18}}} \tag{4}$$

where the shift now accounts for the combined motion of both masses in concert. The magnitude of this shift would then be ~0.5%, which is likely beyond the resolution of our Raman system.

4 | DISCUSSION

Three types of particulates were identified by Raman spectroscopy in distinct regions relative to the craters produced by laser impingement on cerium targets: CeO_2 from both CW heating and laser ablation, poorly crystallized cerium oxide phase from laser ablation, and hexagonal Ce_2O_3 from CW heating. These results indicate that there is a thermodynamic effect on the crystallinity and speciation of cerium oxides as well as the morphology of the crater specific to these oxides. Although the CW heating temperature is difficult to measure, based on the observed features that appear due to melt around the observed Ce_2O_3 particulate (see Figure 1b), it likely exceeded 1000 K. This is in contrast to the PLA where initial temperatures are extremely high (>10 000 K) but drop to comparable temperatures within microseconds or tens of microseconds.

It is shown that the cerium sesquioxide phase seen here, as formed with CW heating, is similar to that formed by other forms of annealing.[10,11] The absence of Ce_2O_3 in the PLA experiments suggests that a relatively long heating time is needed to promote the formation of this reduced phase. However, as shown in previous work,[10,11] the formation of hexagonal Ce_2O_3 while heating is greatly favored in reducing environments, such as H_2, which explains why both CeO_2 and Ce_2O_3 are concurrently seen here when formed in O_2.

The fluorite mode is shifted to lower wavenumber, and peak broadening in collected Raman spectra is consistent with reported changes in the lattice constant and the

formation of vacancies.[6,20,23] The process of reduction and reoxygenation of CeO_2 is shown to induce vacancies that led to a transformation into Ce_2O_3.[13] In this work, we explored the reverse direction where scarce oxygen interacts with cerium metal in a relatively slow process of constant CW heating. This may provide the right conditions in the cerium melt to contribute to the gradual incorporation of oxygen with a high density of vacancies that over the length of heating approach a stable stoichiometry of Ce_2O_3. Both Ce^{3+} and oxygen vacancies are active sites for reactions such as hydrolysis[31] and catalysis.[20,32]

5 | CONCLUSION

Subjecting cerium in the presence of oxygen to different thermodynamic conditions generated by pulsed and CW lasers leads to various oxides with distinct structures and compositions. Future studies could investigate the role of surface melt in the formation of A-type sesquioxide that was observed only in the melted region of the crater. Furthermore, our results (e.g., the $Ce_2{}^{18}O_3$ Raman spectrum from CW laser synthesis) suggest a simpler synthesis method for Ce_2O_3. We have demonstrated a bottom–up method to synthesize and characterize a variety of cerium oxide structures that presents a potential step forward for quality control of their industrial manufacture and the expansion of their utility.

ACKNOWLEDGMENTS

The authors would like to thank Charlotte Eng for her XRD work provided for this study. This work was performed under the auspices of the U.S. Department of Energy by Lawrence Livermore National Laboratory under contract DE-AC52-07NA27344 and is supported by LLNL Strategic Initiative LDRD (project 20-SI-006). This work was released under IM release no. LLNL-JRNL-843195.

CONFLICT OF INTEREST STATEMENT

The authors declare they have no conflicts of interest.

ORCID

Alexander W. Auner https://orcid.org/0000-0003-3448-8641

REFERENCES

1. Kolodiazhnyi T, Sakurai H, Avdeev M, Charoonsuk T, Lamonova KV, Pashkevich YG, et al. Giant magnetocapacitance in cerium sesquioxide. Phys Rev B. 2018;98(5):54423. https://doi.org/10.1103/PhysRevB.98.054423
2. Matz O, Calatayud M. H_2 dissociation and oxygen vacancy formation on Ce2O3 surfaces. Top Catal. 2019;62(12):956–67. https://doi.org/10.1007/s11244-019-01183-0
3. Zhang C, Xu Y, Lv C, Bai L, Liao J, Zhai Y, et al. Amorphous engineered cerium oxides photocatalyst for efficient nitrogen fixation. Appl Catal B Environ. 2020;264:118416. https://doi.org/10.1016/j.apcatb.2019.118416
4. Pereira A, Blouin M, Pillonnet A, Guay D. Structure and valence properties of ceria films synthesized by laser ablation under reducing atmosphere. Mater Res Express. 2014;1(1):15704. https://doi.org/10.1088/2053-1591/1/1/015704
5. Gong W, Zhang R, Chen Z. Thermodynamic modelling and applications of Ce–La–O phase diagram. Trans Nonferrous Met Soc China. 2011;21(12):2671–76. https://doi.org/10.1016/S1003-6326(11)61109-6
6. Murali A, Lan Y-P, Sohn HY. Effect of oxygen vacancies in non-stoichiometric ceria on its photocatalytic properties. Nano-Struct Nano-Objects. 2019;18:100257. https://doi.org/10.1016/j.nanoso.2019.100257
7. Ackermann S, Sauvin L, Castiglioni R, Rupp JLM, Scheffe JR, Steinfeld A. Kinetics of CO_2 reduction over nonstoichiometric ceria. J Phys Chem C. 2015;119(29):16452–61. https://doi.org/10.1021/acs.jpcc.5b03464
8. Wheeler VM, Zapata JI, Kreider PB, Lipiński W. Effect of non-stoichiometry on optical, radiative, and thermal characteristics of ceria undergoing reduction. Opt Express. 2018;26(10):A360–73. https://doi.org/10.1364/OE.26.00A360
9. Dejoie C, Yu Y, Bernardi F, Tamura N, Kunz M, Marcus MA, et al. Potential control of oxygen non-stoichiometry in cerium oxide and phase transition away from equilibrium. ACS Appl Mater Interfaces. 2020;12(28):31514–21. https://doi.org/10.1021/acsami.0c08284
10. Avisar D, Livneh T. The Raman-scattering of A-type Ce_2O_3. Vib Spectrosc. 2016;86:14–16. https://doi.org/10.1016/j.vibspec.2016.05.006
11. Sethi A, Slimak JE, Kolodiazhnyi T, Cooper SL. Emergent vibronic excitations in the magnetodielectric regime of Ce_2O_3. Phys Rev Lett. 2019;122(17):177601. https://doi.org/10.1103/PhysRevLett.122.177601
12. Hamm CM, Alff L, Albert B. Synthesis of microcrystalline Ce_2O_3 and formation of solid solutions between cerium and lanthanum oxides. Zeitschrift für Anorg und Allg Chemie. 2014;640(6):1050–53. https://doi.org/10.1002/zaac.201300⟨3:hyphenbreak ⟩⟨/3:hyphenbreak⟩663
13. Xiao W, Guo Q, Wang EG. Transformation of CeO_2(111) to Ce_2O_3(0001) films. Chem Phys Lett. 2003;368(5):527–31. https://doi.org/10.1016/S0009-2614(02)01889-4
14. Wautelet M. Laser-assisted reaction of metals with oxygen. Appl Phys A. 1990;50(2):131–39. https://doi.org/10.1007/BF00343408
15. Bunkin FV, Kirichenko NA, Lukyanchuk BS, Simakhin AV, Shafeev GA, Nánai L, et al. On the characteristics of the oxidation of vanadium effected by a continuous beam of laser light. Acta Phys Hungarica. 1983;54(1):111–18. https://doi.org/10.1007/BF03158697
16. Ursu I, Nanu L, Dinescu M, Hening A, Mihailescu IN, Nistor LC, et al. Vanadium oxidation as a result of CW CO_2 laser irradiation in atmospheric air. Appl Phys A. 1984;35(2):103–8. https://doi.org/10.1007/BF00620638
17. Palatnikov M, Shcherbina O, Frolov A, Pavlikov V, Chufyrev P, Makarova OV, et al. Formation of fractal micro- and nano-structures in ceramic tantalum pentoxide under concentrated flux of light and their effect on thermal expansion.

Integr Ferroelectr. 2009;108(1):89–97. https://doi.org/10.1080/10584580903324477

18. Liu XQ, Han XD, Zhang Z, Ji LF, Jiang YJ. The crystal structure of high temperature phase Ta_2O_5. Acta Mater. 2007;55(7):2385–96. https://doi.org/10.1016/j.actamat.2006.11.031
19. Filotti L, Bensalem A, Bozon-Verduraz F, Shafeev GA, Voronov VV. A comparative study of partial reduction of ceria via laser ablation in air and soft chemical route. Appl Surf Sci. 1997;109–110:249–52. https://doi.org/10.1016/S0169-4332(96)00665-4
20. Schmitt R, Nenning A, Kraynis O, Korobko R, Frenkel AI, Lubomirsky I, et al. A review of defect structure and chemistry in ceria and its solid solutions. Chem Soc Rev. 2020;49(2):554–92. https://doi.org/10.1039/C9CS00588A
21. Taniguchi T, Watanabe T, Sugiyama N, Subramani AK, Wagata H, Matsushita N, et al. Identifying defects in ceria-based nanocrystals by UV resonance Raman spectroscopy. J Phys Chem C. 2009;113(46):19789–93. https://doi.org/10.1021/jp9049457
22. Guo M, Lu J, Wu Y, Wang Y, Luo M. UV and visible Raman studies of oxygen vacancies in rare-earth-doped ceria. Langmuir. 2011;27(7):3872–77. https://doi.org/10.1021/la200292f
23. Wu Z, Li M, Mullins DR, Overbury SH. Probing the surface sites of CeO_2 nanocrystals with well-defined surface planes via methanol adsorption and desorption. ACS Catal. 2012;2(11):2224–34. https://doi.org/10.1021/cs300467p
24. Pushkarev VV, Kovalchuk VI, d'Itri JL. Probing defect sites on the CeO_2 surface with dioxygen. J Phys Chem B. 2004;108(17):5341–48. https://doi.org/10.1021/jp0311254
25. Burton MA, Auner AW, Crowhurst JC, Boone PS, Finney LA, Weisz DG, et al. The effect of oxygen concentration on the speciation of laser ablated uranium. Sci Rep. 2022;12(1):4030. https://doi.org/10.1038/s41598-022-07834-9
26. McBride JR, Hass KC, Poindexter BD, Weber WH. Raman and X-ray studies of $Ce_{1-x}RE_xO_{2-y}$, where RE = La, Pr, Nd, Eu, Gd, and Tb. J Appl Phys. 1994;76(4):2435–41. https://doi.org/10.1063/1.357593
27. Weckhuysen BM, Jehng J-M, Wachs IE. In situ Raman spectroscopy of supported transition metal oxide catalysts: $^{18}O_2$–$^{16}O_2$ isotopic labeling studies. J Phys Chem B. 2000;104(31):7382–87. https://doi.org/10.1021/jp000055n
28. Lv J, Li G, Guo S, Shi Y. Raman scattering from phonons and electronic excitations in UO_2 with different oxygen isotopes. J Raman Spectrosc. 2016;47(3):345–49. https://doi.org/10.1002/jrs.4785
29. Penkala B, Aubert D, Kaper H, Tardivat C, Conder K, Paulus W. The role of lattice oxygen in CO oxidation over $Ce_{18}O_2$-based catalysts revealed under operando conditions. Catal Sci Technol. 2015;5(10):4839–48. https://doi.org/10.1039/C5CY00842E
30. Lopez HF, Mendoza H. Temperature effects on the crystallization and coarsening of nano-CeO_2 powders. ISRN Nanomater. 2013;2013:208614. https://doi.org/10.1155/2013/208614
31. Chueh WC, McDaniel AH, Grass ME, Hao Y, Jabeen N, Liu Z, et al. Highly enhanced concentration and stability of reactive Ce^{3+} on doped CeO_2 surface revealed in operando. Chem Mater. 2012;24(10):1876–82. https://doi.org/10.1021/cm300574v
32. Nolan M, Parker SC, Watson GW. The electronic structure of oxygen vacancy defects at the low index surfaces of ceria. Surf Sci. 2005;595(1–3):223–32. https://doi.org/10.1016/j.susc.2005.08.015

SUPPORTING INFORMATION

Additional supporting information can be found online in the Supporting Information section at the end of this article.

How to cite this article: Auner AW, Burton MA, Nagel LA, Crowhurst JC, Weisz DG, Knight KB. A comparative study of cerium oxides formed by pulsed laser ablation and continuous wave laser heating. J Am Ceram Soc. 2024;107:514–521. https://doi.org/10.1111/jace.19429